Polymer Single Crystal-Decorated Superhydrophobic Buckypaper with Controlled Wetting and Conductivity

Eric D. Laird, Wenda Wang, Shan Cheng, Bing Li, Volker Presser, Boris Dyatkin, Yury Gogotsi, and Christopher Y. Li*

A. J. Drexel Nanotechnology Institute and Department of Materials Science and Engineering, Drexel University, Philadelphia, Pennsylvania 19104, United States

CNT films and electrodes both with and without surface modification have been produced in numerous ways, including directed growth from a catalyst substrate,[1] drop casting,[2] vacuum deposition,[3] vacuum decomposition of silicon carbide,[4] electrodeposition,[5] hydroentangling,[6] Langmuir—Blodgett monolayer deposition,[7,8] and inkjet printing.[9,10] The properties of CNT films strongly depend on the nanotube quality and the processing methods employed. Each technique has its own advantages in terms of production, alignment, throughput, and applications. For example, vacuum filtration has been used to yield conductive CNT films showing nearly complete transparency in the visible spectrum and voltage-dependent transparency in the infrared range.[3] Hydroentanglement of CNT can be used to improve Young's modulus, creep resistance, conductivity, and reversible charge storage capacity.[6] The functionality of CNT films can be further extended by incorporating a polymer coating: Lau *et al.* showed that a CNT forest produced by guided growth and coated with a hydrophobic polymer had superhydrophobic properties.[11]

Free-standing CNT films, often referred to as buckypaper, show exceptional mechanical and electrical properties.[12] One drawback of buckypaper and similar CNT-based films is, however, that once CNTs are aggregated, the pore size of the paper is fixed, thus limiting the options for further functionalization. In some cases it is possible to further constrict pore sizes to tailor properties. For instance, mechanically confined and stressed CNT films show interesting properties like uniform relaxation; regular corrugated patterns can thus be achieved.[13,14] Solvent evaporation from isolated islands of CNT forests has been used to collapse them into a bell shape with an increased packing density and volume-specific capacitance.[15]

ABSTRACT
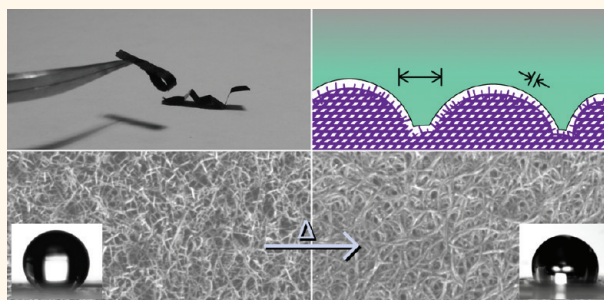
Herein we report fabrication of uniform, free-standing nanohybrid buckypaper with high carbon nanotube (CNT) contents (13—70%) using polymer single crystal-decorated CNTs as the precursor. Polyethylene single crystals were periodically grown on CNT surfaces, forming a nanohybrid shish kebab (NHSK) structure. Vacuum filtering a NHSK suspension led to polymer single crystal-decorated buckypaper (named as NHSK paper) with a wide range of CNT contents and uniform CNT dispersion. Porosity, surface roughness, and conductivity of NHSK paper can be controlled by tuning the polymer single crystal size. Because of the hierarchical roughness created by intra- and inter-NHSK nanostructure, NHSK paper with controlled kebab size exhibits both superhydrophobicity and high surface water adhesion, which mimics the rose petal effect. We anticipate that this unique NHSK paper can find applications in sensors, electrochemical devices, and coatings.

Widening the pore size of buckypaper, on the other hand, is not possible using such techniques. CNT forests do allow ample space between the CNTs. However, in this case, CNTs are completely separated from each other and the membranes are not free-standing or have low mechanical properties. It is attractive to fabricate free-standing CNT paper with separated CNTs and tunable pore size. The latter would allow easy functionalization and infiltration of proteins, polymers, ions, *etc.* to the paper for various applications such as electrochemical devices and sensors.
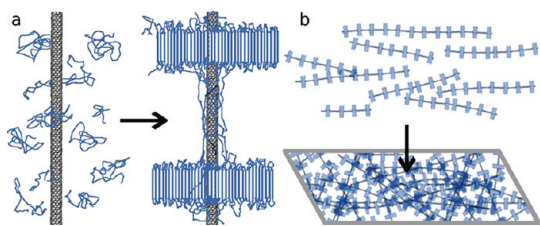
Herein we demonstrate that we can achieve this goal using polymer single crystal

Scheme 1. Flowchart for the formation of NHSK films. (a) Polymer is solution-crystallized using a CNT as the heterogeneous nucleus to form NHSK. (b) NHSK in solution are vacuum-deposited through a membrane filter to form NHSK paper

(PSC)-decorated CNTs. PSCs are typically 2D lamellae with folded polymer chains and they can be used as spacers to separate individual CNTs and decorate nanoparticles.[16−20] The strategy we adopted is using our recently developed hybrid structure, "nano-hybrid shish kebab" (NHSK), instead of pristine CNTs, as the building block to fabricate buckypaper (Scheme 1).[21,22] CNTs serve as epitaxial nucleation sites for polymer single crystals. Being confined to the surface of the CNT, the early crystallization growth is favored for the oriented polymer chains, resulting in lamellae that are primarily perpendicular to the CNT axis. The result is a semiperiodic crystal arrangement, with an appearance similar to "beads on a string". The nanostructured material bears close resemblance to the classical polyethylene (PE) "shish-kebabs" first described by Pennings,[23−25] and was therefore termed NHSK. The "shish" in these materials is the CNT, which ultimately becomes both the support material for these films as well as the conductive filler. This technique was demonstrated using single-walled carbon nanotubes (SWCNT), multiwalled carbon nanotubes, and carbon fibers.[26−28] From Scheme 1, it is apparent that, because the 2D polymer lamellae "kebabs" are orthogonal to the CNT, using the vacuum deposition, buckypaper can be fabricated where the lamellae can serve as the "spacers" to separate individual CNTs, allowing pore size control of the paper. Furthermore, various types of NHSKs have been reported recently. For example, we showed that amphiphilic block copolymer with a monodisperse periodicity of 12 ± 0.9 nm could be decorated on a single CNT by spin-coating crystalline diblock copolymers over the SWCNT.[29] Other reported polymer materials that have been crystallized into "kebabs" include nylon 66 and poly(L-lysine).[30] CNTs have also been reported in several studies to initiate transcrystallinity of poly(vinyl alcohol)[31] and isotactic polypropylene.[32,33] These various types of NHSKs provide a possible tool box to fabricate buckypaper with controlled functionality for targeted applications.

In this work, hybrid PE NHSK buckypaper (from now on, referred to as NHSK paper) with versatile surface features, wetting properties, and conductivity were produced at various polymer loadings. These hybrid
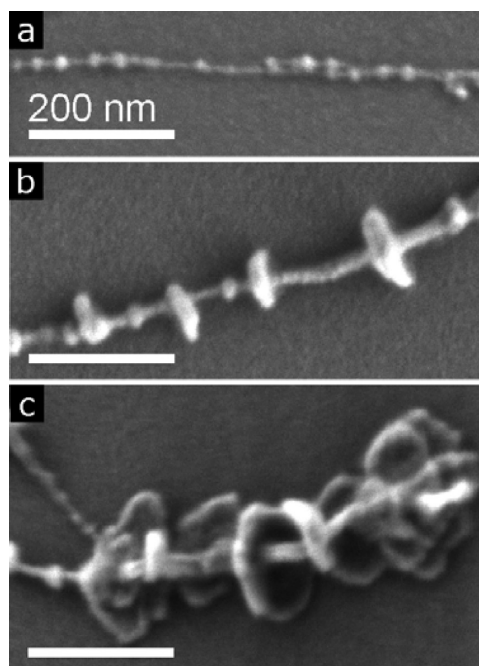

Figure 1. SEM micrographs of NHSK with (a) 70% SWCNT, (b) 25% SWCNT, and (c) 13% SWCNT content.

materials have SWCNT contents that are much higher than in most polymer−nanotube nanocomposites. NHSK paper in this study was controlled to be of the order of 5−20 μm in thickness, although thicker films can be easily achieved. All the NHSK papers are highly flexible and can be made freestanding as desired, and show high water contact angle, high surface water adhesion, and tunable electrical conductivity.

RESULTS AND DISCUSSION

NHSK Paper Fabrication and General Characteristics. Five batches of NHSK with varying PE contents were fabricated following the procedure discussed in the experimental section. NHSK structure was formed in all cases. The average kebab crystal diameter ranges from ∼17 to 94 nm, and the mean intra-NHSK spacing (defined as the spacing between the adjacent kebab crystals along a CNT, also known as the NHSK period) was found to be 35−68 nm. Figure 1 shows SEM micrographs of NHSKs with different PE/SWCNT contents. It is clear that, with decreasing SWCNT contents in NHSK, the PE kebab crystal size increases. Detailed information regarding PE crystal size is listed in Table 1, along with other NHSK paper properties. The diameters and intra-NHSK spacings can be expected to follow a log-normal distribution[34] (see Supporting Information for comprehensive analysis). The mean diameter of the PE kebab was found to be an indicator of the final PE content. In general, the intra-NHSK spacing distributions were found to be more uniform across different batches of NHSK than crystal diameter distributions at the dilute concentrations used in this study. The reason for this is

TABLE 1. Characteristics of Buckypaper and NHSK Paper Measured in This Study[a]

wt % SWCNT =	100	70	52	25	20	13
D (nm)	N/A	17.6	35.0	54.8	80.3	93.9
d_{intra} (nm)	N/A	35.4	60.3	57.2	70.7	68.0
d_{inter} (nm)	N/A	671	470	419	495	368
θ (deg)	82.2	116.6	137.9	152.3	138.8	123.9
$\theta_{ADV}/\theta_{REC}$ (deg)	93.7/41.2	123.6/50.1	150.6/64.7	170.9/55.9	147.8/43.8	138.0/55.1
σ (S cm^{-1})	1,930	267	78.5	21.0	41.4	2.64

[a] Kebab diameter (D), intra-NHSK spacing (d_{intra}), and inter-NHSK spacing (d_{inter}), water CAs (θ), advancing (θ_{ADV}) and receding (θ_{REC}) CAs, and conductivity (σ) of SWCNT buckypaper and NHSK films are shown in the table.
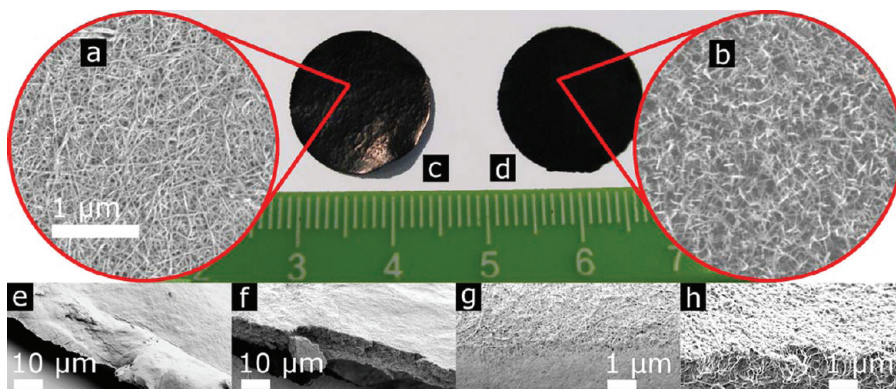

Figure 2. Comparison of SWCNT buckypaper and NHSK paper. (a,b) SEM image of top surfaces of vacuum-deposited SWCNT buckypaper (a) and NHSK buckypaper (b). (c,d) Optical images of the as-deposited SWCNT (c) and NHSK paper with 25 wt % SWCNT content (d) films. Light is easily reflected off of the surface of SWCNT buckypaper, but is scattered effectively from the NHSK buckypaper surface. (e,f) Freeze-fractured surfaces of (e) SWCNT buckypaper and (f) NHSK buckypaper with 25 wt % SWCNT. (g) Details of the fracture surface of SWCNT buckypaper. (h) Details of a 13 wt % SWCNT content NHSK paper cross-section.

that in dilute solution, the crystal density along the CNT is controlled by nucleation rate and early stage crystallization. After a crystal nucleus of appropriate size is grown on a CNT surface, the remaining polymer in the local area is depleted as it is incorporated into the heterogeneously nucleated polymer crystal *via* ordinary crystal growth.

These NHSKs were deposited into films to fabricate NHSK paper and the PE contents in each paper were confirmed by thermogravimetric (TGA) experiments (see Supporting Information for details). Pure SWCNT was also used to fabricate buckypaper. Figure 2 shows the visual appearance and SEM images of the top and side surface of buckypaper (Figure 2a,c,e, and g) and NHSK paper (Figure 2b,d,f, and h) fabricated by vacuum filtration. The visual appearance of SWCNT buckypaper is much more reflective than that of the NHSK paper (Figure 2 panels c and d, respectively). This is due to the efficient light scattering of the porous surface of the NHSK, which will be discussed in more detail later. Figure 2a shows that SWCNTs aggregates into bundles that are aligned relatively parallel to the buckypaper surface. The average diameter of these bundles is ~13.2 nm, with some bundle diameters reaching almost 80 nm estimated using Image J. However, in the NHSK paper case, SWCNTs were mostly separated into

individual tubes by the kebab crystals, as shown in Figure 2b. Note that the bundle size of the SWCNTs in NHSKs can be controlled by controlling the solution crystallization conditions.[17,22] NHSKs are also aligned relatively parallel to the paper surface while PE lamellar crystals are generally perpendicular to the film surface. This indicates that the overall surface roughness of the NHSK paper can be tuned by controlling the PE crystal size. A detailed SWCNT orientation study will be presented in the following section. The cross-section of buckypaper in Figure 2, for example, shows a dense structure while that of NHSK paper clearly reveals the porous nature of the latter (Figure 2f,h). The thickness of the NHSK paper is approximately 10 μm.

SAXS Determination of NHSK Alignment. SAXS has been used to study the structural anisotropy of the NHSK paper. Pujari *et al.* described the relative orientation of multiwalled CNT in a viscous medium under shear flow.[35] This calculation may also be adopted to find the relative orientation of SWCNT in NHSK papers. For a material with filler oriented anisotropically in the $x-z$ plane, the anisotropy can be described through the second moment tensor along the $\xi-\zeta$ plane of the SAXS pattern[36] (the reciprocal space projection of $x-z$), which is defined as the total weighted intensity along
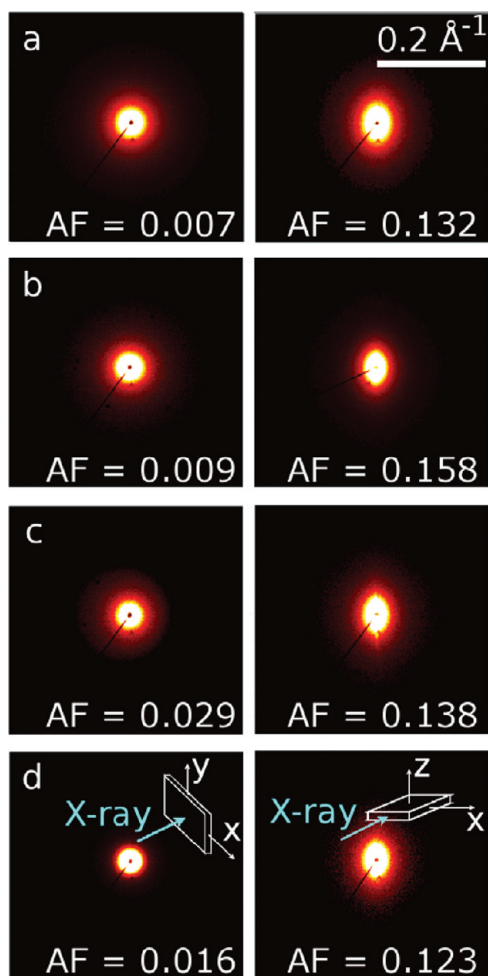
Figure 3. Through-plane (left) and in-plane (right) SAXS patterns of films of various SWCNT loadings. (a) SWNT buckypaper; (b) 70 wt % SWCNT NHSK paper; (c) 25 wt % SWCNT NHSK paper; (d) 13 wt % SWCNT NHSK paper. Annotation shows the calculated anisotropy factor (AF) for each film. Left column shows $\xi-\eta$ scattering patterns while the right column shows $\xi-\zeta$ plane scattering patterns. The horizontal axis is ξ direction for all the patterns.

all scattering vectors **q** as shown in eq 1:

$$\langle \mathbf{qq} \rangle_{\xi\zeta} = \begin{pmatrix} \langle q_{\xi}q_{\xi} \rangle & \langle q_{\xi}q_{\zeta} \rangle \\ \langle q_{\xi}q_{\zeta} \rangle & \langle q_{\zeta}q_{\zeta} \rangle \end{pmatrix}$$

$$\equiv \frac{\iint \mathbf{q}\cdot\mathbf{q}I(\mathbf{q})\,d\mathbf{q}_{\xi}\,d\mathbf{q}_{\zeta}}{\iint q^2 I(\mathbf{q})\,d\mathbf{q}_{\xi}\,d\mathbf{q}_{\zeta}} \quad (1)$$

where I is the intensity at **q**. Similarly, the second moment tensor in the $\xi-\eta$ plane (reciprocal to the $x-y$ plane) is defined as

$$\langle \mathbf{qq} \rangle_{\xi\eta} = \begin{pmatrix} \langle q_{\xi}q_{\xi} \rangle & \langle q_{\xi}q_{\eta} \rangle \\ \langle q_{\xi}q_{\eta} \rangle & \langle q_{\eta}q_{\eta} \rangle \end{pmatrix}$$

$$\equiv \frac{\iint \mathbf{q}\cdot\mathbf{q}I(\mathbf{q})\,d\mathbf{q}_{\xi}\,d\mathbf{q}_{\eta}}{\iint q^2 I(\mathbf{q})\,d\mathbf{q}_{\xi}\,d\mathbf{q}_{\eta}} \quad (2)$$

From the entries of these tensor matrices, an "anisotropy factor" (AF) can be calculated, which describes the degree of alignment of the SWCNT in the film. As each
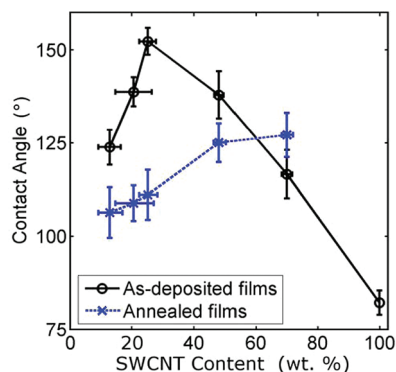

Figure 4. CA *versus* SWCNT content for NHSK paper and buckypaper films for as-deposited and annealed samples: *x*-Error bars represent uncertainty in wt %; *y*-error bars represent standard deviations of at least eight droplets.

entry in the tensor matrix is normalized by the total scattering intensity, this anisotropy factor must vary between 0 for a completely disoriented material and 1 for a material with perfect alignment.

$$\mathrm{AF} = \sqrt{(\langle q_{\xi}q_{\xi} \rangle - \langle q_k q_k \rangle)^2 + 4\langle q_{\xi}q_k \rangle^2} \quad (3)$$

Here, k denotes either η or ζ as required. Buckypaper and NHSK papers have ring orientation about z (z is the NHSK normal), so the anisotropy factor is expected to reduce to zero for the product moment of area entries $\langle q_{\xi}q_k \rangle$. Figure 3 shows SAXS patterns for SWCNT buckypapers and NHSK papers, as well as the calculated AFs. CNTs and NHSKs are isotropic along xy plane while the anisotropy factor of buckypaper and NHSK paper along xz plane was found to be moderate ($\sim$0.1 to 0.15) in all cases, as no effort was made to control the orientation of the material as it was deposited. For the NHSK paper with the lowest SWCNT content, the anisotropy factor is lower than the other films. We attribute this to the increased influence of the polymer single crystals because they begin to collapse onto the NHSK paper surface, affecting the scattering pattern.

Droplet Wetting of NHSK Paper. The unique structure of the NHSK paper and the orthogonal orientation of the kebab crystal with the paper surface motivated us to study the wetting behavior of NHSK paper which we expected to differ from that of other carbon films.[37,38] Using the sessile drop technique, the contact angles (CAs) of water drops on the surfaces of films were measured to investigate the nano-roughness effect on the wetting properties of the material. Water drops of 2 μL were placed on the surfaces of the films. Figure 4 shows the plot of CA *versus* SWCNT contents while Figure 5 shows SEM micrographs of the surface of the corresponding paper. SWCNT buckypaper (Figure 5a) shows a CA of 84.7° while the NHSK paper with the highest CNT content (70 wt %, Figure 5b) has a CA of 114.4°. As the CNT content of NHSK paper decreased, the kebab size increased, and so did the surface roughness.
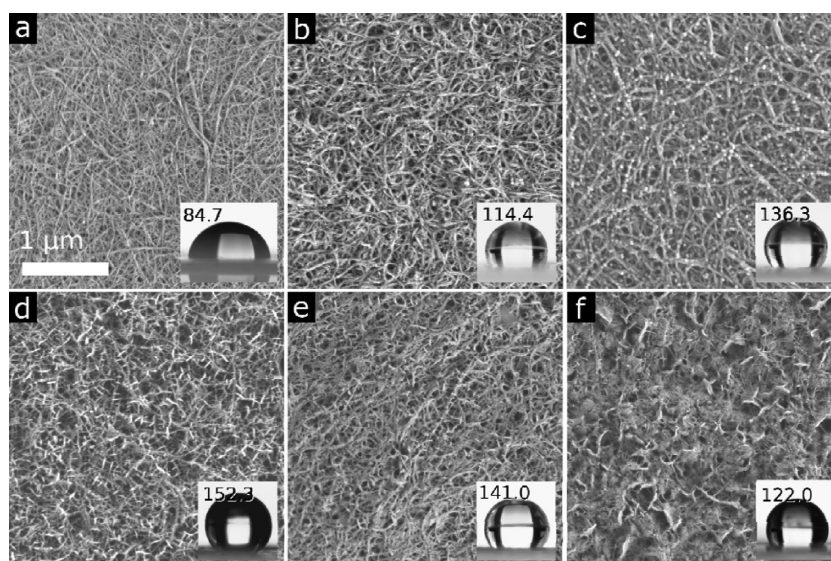
Figure 5. SEM images of films surfaces and optical images of sessile drops for the films. (a) SWCNT buckypaper. (b–f) SWCNT NHSK films with 70 (b), 52 (c), 25 (d), 20 (e), and 13 wt % SWCNT (f). Inset images are 2 μL water drops on SWCNT buckypaper and NHSK paper surfaces, with CAs for these droplets.

In turn, CA increased to 136.3° and 152.3° for 52 wt % and 25 wt % CNTs, respectively (Figure 5c,d). Superhydrophobic behavior was then achieved as the CA was greater than 150° for NHSK paper with 25 wt % CNT. This is consistent with reports on using CNT as well as polymer nanofibers to create superhydrophobic surfaces.[39–41] As the CNT content further decreased, however, CA decreased to 141.0° and 122.0° for NHSK paper with 20 wt % and 13 wt % CNT, respectively. SEM imaging showed that in these two cases, PE kebab crystals were relatively large and were not able to maintain orthogonal orientation with respect to the NHSK paper; these large lamellar crystal fold/collapsed onto the paper surface, which decreased the surface roughness, reducing the CA.

A rotational stage was used to measure the angles at which water droplets rolled off the surface of the material. All the NHSK paper, including the superhydrophobic one, showed high water adhesion; water droplets tended to stick onto the surface even when the NHSK paper was turned upside down. NHSK paper with 25 wt % SWCNT is of particular interest because it exhibits both high surface water adhesion and superhydrophobicity. At this point it is appropriate to consider how a water droplet wets the surface of such a film. The Cassie–Baxter state, which is common for porous hydrophobic films, is characterized by a high advancing CA and low CA hysteresis. This possibility was eliminated in the present case, because the hysteresis between advancing and receding CAs for these materials was found to be very high (Table 1). The Wenzel state for the NHSK network was considered next. Given the highly porous nature of these films and the intrinsic hydrophobicity of PE, this case was also difficult to rationalize. If the films are hydrophobic
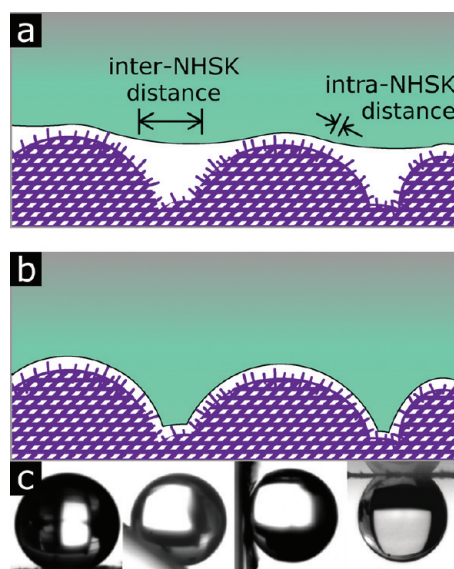

Figure 6. Wetting of NHSK paper by water droplets. (A) Hypothetical Cassie–Baxter wetting state and (B) "Petal Effect" wetting. (C) Appearance of 2 μL droplets on the superhydrophobic (25 wt % SWCNT) NHSK film, held at (from left to right) 0, 45, and 90° angles of inclination, and a 5 μL droplet suspended upside down from the same film.

enough to prevent the droplet from being fully absorbed, such droplet penetration into the depth of the film is not feasible. The CA hysteresis is considerable even for materials in a Wenzel wetting regime, although it is not without precedent.[42] The CA is also too high for the Wenzel state. Therefore, the "Cassie impregnating wetting state"[43] (which includes "rose petal" effect[44]) is appropriate to describe the wetting behavior of the NHSK paper with 25 wt % SWCNTs (see Figure 6).

For surfaces exhibiting the Cassie-impregnating wetting state, there are typically multiple levels of
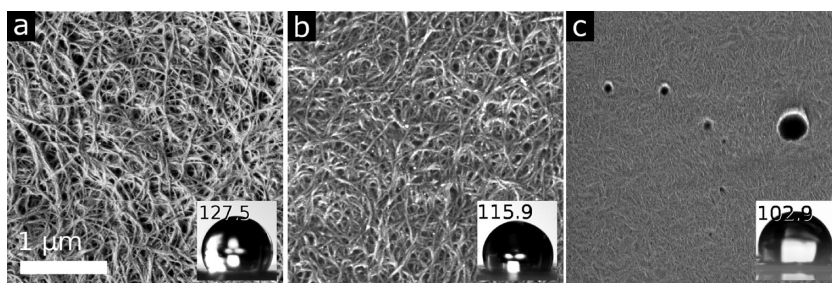
Figure 7. Surface structure of NHSK films after annealing above the PE melting transition and subsequent quenching in liquid nitrogen and their associated CAs: (a) 70%; (b) 25%; (c) 13% SWCNT. Insets in panels a−c are the shapes of 2 μL sessile drops and CAs for these drops.

roughness due to hierarchical surface structure. Water droplet contact lines can reach down into the larger-scale features of the surface (Wenzel), but cannot penetrate into nanoscale asperities (Cassie), as shown in Figure 6. Therefore, a Cassie impregnating wetting state can also be considered as the Wenzel^m−Cassie^n state, where the superscripts denote the corresponding length scale, micro- or nano-, respectively.[45,46] In the case of NHSK paper, the hierarchical roughness is due to inter- and intra-NHSKs. The quasi-periodic arrangement of the kebab crystals with a 50 nm kebab spacing contributes to the nanoscale roughness; BET analysis showed an average pore size of 31 nm and a surface area of ∼81 m^2/g. 2D random packing of these NHSKs leads to an inter-NHSK roughness that is ∼619 nm obtained by imaging analysis (microroughness). As shown in Figure 6b, water droplets are suspended above the single crystals due to intra-NHSK roughness. However, inter-NHSK produces an undulating surface irregularity which is observable to the water drop, leading to high adhesion force. The adhesion force of the superhydrophobic (25 wt % SWCNT) film was greater than 49 μN based on the ability of the surface to overcome the droplet's body weight and suspend droplets as large as 5 μL upside down. Note that both in nature and in microfabricated surfaces, the rose petal effect is typically observed on surfaces with dual roughness on tens of micrometers and submicrometer length scales, which are similar to the present system. From the above discussion, it is also clear that one can independently tune the structural features (e. g., for a mircofabricated surface, pillar size, aspect ratio, and periods) at different length scales as well as the surface chemistry in order to achieve the Wenzel^m−Cassie^n state.[44−46]

The apparent CA of the NHSK paper can also be estimated based on the following equation:[44−47]

$$\cos \theta_{impr}^{C} = f(r \cos \theta^{Y} + 1) - 1 \qquad (4)$$

where θ_{impr}^{C} is the observed CA, θ^{Y} is the Young CA for PE single crystals (taken as 94°),[48] f is the solid (or wetted) fraction of the nanoscale feature, and r is the microscale Wenzel roughness. (In this case, f can be estimated as the ratio between single crystal

thickness (∼10 nm) and the kebab periods (∼60 nm). The Wenzel roughness is the same as the roughness factor for the microstructure. We estimate this value to be approximately 1.16 as explained in the Supporting Information). The calculated apprarent CA is 147.9°, which is close to the observed value.

Dynamic methods were also used to investigate the advancing and receding CAs. Advancing CAs were measured by analyzing droplets that were expanded by increasing volume. Receding CAs were measured by droplet evaporation. This method allowed multiple contact line unpinning events to be observed: the metastable minimum receding CA could therefore be determined accurately.[49] The advancing CAs were found to be above 120° for all NHSK films, with the superhydrophobic NHSK paper demonstrating an advancing CA of over 170°. The receding CAs were less than 70° in all cases. This data are summarized in Table 1. Droplet pinning due to the high adhesion energy was responsible for this high hysteresis. Such high CA hysteresis is consistent with the free energy cost of rearranging a continuous contact line over a rough surface.[50] As the droplet prepares to shift into a new orientation, it must arrange its interfacial molecules in such a way as to minimize the surface energy of the three-phase contact line. In the case of NHSK paper, because polymer single crystals are flexible in nature due to the thinness of the lamellae, they may also bend/deform, which further increases CA hysteresis.[51]

NHSK paper was thermally treated above the PE crystal melting temperature to further confirm the role of the polymer single crystals on the water CA and to investigate the potential of NHSK paper as a thermally responsive material. Figure 7 shows representative SEM images of the annealed surface; the kebab crystal disappeared after annealing, which is due to the melting of PE crystals. Molten PE filled in the void regions of NHSK paper so the overall roughness of the film decreased as evidenced by the SEM images. The melting of PE crystals also affected CAs of NHSK paper and Figure 4 shows the plot of CA versus SWCNT content of the NHSK paper after annealing. For most NHSK samples, CA decreased after annealing, and CAs of
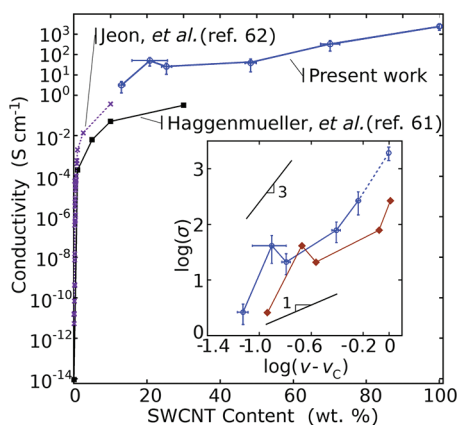
Figure 8. In-plane conductivity as a function of SWCNT loading. x-Error bars represent the uncertainty in wt %; y-error bars are standard deviations of five samples measured in four-point configuration. Inset: log−log plot of NHSK in-plane conductivity (σ) vs SWCNT volume percent (v) above critical percolation threshold (v_c) which was taken to be 0.6 vol % following ref 52. The dashed line connects to SWCNT buckypaper. SWCNT volume fractions were calculated with (filled diamond) and without (open circles) the pore volume of the NHSK paper.

annealed NHSK paper with 25, 20, and 13 wt % SWCNT samples are quite close. This is because the surface of the NHSK paper is mostly covered by PE after annealing (Figure 7c). Of interest is that the annealing treatment increased the CA for the NHSK paper with 70 wt % SWCNT. This may be because upon melting, PE melt allowed adjacent CNT to aggregate. Because of relatively low PE contents, there was not enough PE to fill in the void region, leading to CA increase.

Conductivity of NHSK Paper and Buckypaper. Porous conductive films are desirable materials for batteries and supercapacitors, but in aqueous cells the operating voltage is limited by the onset of hydrolysis, which can be catalyzed by the surface functional groups on CNTs. In some instances it may be possible to take advantage of the insulating functionalization to allow the films to operate reliably in environments where high voltage swings or electromagnetic noise may be anticipated.[52] NHSK functionalization allows the pore sizes to be adjusted based on the crystal diameter, for applications such as glucose monitoring *via* glucose oxidase-enabled electrochemical processes.[53,54] Figure 8 shows the plot of conductivity *versus* the SWCNT contents. Above the percolation threshold of a conductive filler in an insulating matrix, the conductivity is expected to scale as a power law as in eq 5.

$$\sigma \propto (v - v_C)^t \qquad (v > v_c) \qquad (5)$$

In this equation, σ is the conductivity and v and v_c are the nanoparticulate volume fraction and nanoparticulate conductivity threshold volume fraction, respectively. Taking a density estimate of 1.6 g/cm^3 for SWCNT of an outer diameter of 1 nm (plus 0.34 nm to account for van der Waals repulsion)[55] and taking a

density of 0.97 g/cm^3 for the PSC phase, the volume fraction of the material can easily be determined for each sample. For the purposes of comparison, literature values of the percolation threshold were adopted to compare the data to previous work and to analyze the critical exponent. The critical exponent, t, is expected to have a value of 2 when filler concentration is above the percolation threshold, as the accumulating conductive filler transitions out of the nonpercolating regime (although the experimental value sometimes is seen to be higher in disordered composites).[56] Far above the percolation threshold however, the critical exponent is expected to have a value of ∼1, as the system is homogeneous and the conductivity increases monotonically.[57−60] This turns out not to be the case for NHSK papers. The confidence interval for the critical exponent is large; nevertheless, we found a critical exponent of 2.0 for NHSK films, despite the fact that the SWCNT content was far above the percolation threshold. Note that if we include the pore volume for the SWCNT volume fraction calculation, the critical exponent is approximately 1.7, which is still much greater than 1. This high exponent can be attributed to the unique structure of NHSK. For homogeneous systems, isotropic replacement of conductive particles with nonconductive filler creates the possibility of separation between adjoining conductive particles. Here, with increasing PE contents, the addition of matrix material is not added indiscriminately; instead it is added to the growth front of the PSC, increasing its diameter as it increases in roughly cylindrical volume (spacer effect). The probability of contacts forming between tubes is therefore dramatically decreased. As a result, the scaling exponent increased. Nevertheless, highly conductive, porous NHSK paper was obtained with controlled conductivity. Figure 8 shows a 2 orders of magnitude increase in conductivity for NHSK paper when compared with CNT−PE nanocomposites.[61] A substantial increase in conductivity was also observed when the system was compared with a very similar system using HiPCO SWCNT from Carbon Nanotechnologies, Inc., prepared by bulk casting from dilute solution of HDPE in DCB.[62] Note that in a CNT-containing polymer nanocomposite system, CNT anisotropy may affect the composite conductivity as recently reported by Winey et al.[63] In our work, SAXS experiments did show moderate orientation of SWCNTs. However, the conductivity change due to structure anisotropy typically is most significant at a low CNT content, and decreases rapidly as the CNT content increases. Because in the present case, high SWCNT contents were used in NHSK paper, the main reason for the increased conductivity can thus be attributed to the openness of the NHSK nanostructure. Further work will test the conductivity of these films after infusing them with insulating and conducting polymers and electrolytes.

CONCLUSIONS

We have successfully demonstrated that highly uniform, free-standing nanohybrid NHSK paper with high CNT contents (13−70%) can be produced using NHSK as the precursor. PE single crystals were solution-grown using CNT as the nucleation sites to form the NHSK, which consists of PE lamellar crystals uniformly decorating CNTs. Upon vacuum filtering NHSK suspension, NHSK paper was formed with the CNT axis being parallel to the film surface and the PE crystals perpendicular to it. All of the NHSK papers were highly flexible and could be made free-standing as desired. The morphology of the NHSK paper was carefully examined using SEM. PE single crystals were then used as a structural control to tune the NHSK paper surface roughness, wetting behavior, and conductivity. With decreasing SWCNT contents, CA first increased to 152.3°, demonstrating a superhydrophobic behavior, and then decreased. This was ascribed to the folding/collapse of overgrowth PE lamellar crystals, as evidenced by SEM and SAXS results. Owing to the two length scales of the surface morphology, (inter- and intra- NHSK), the superhydrophobic NHSK paper also demonstrated high adhesion properties, similar to the interesting "rose petal" effect. Higher conductivity and a higher critical exponent for electrical conductivity were measured for NHSK than would be expected for CNT/polymer nanocomposite, which is because of the separation between CNTs achieved by using polymer single crystal spacers. We anticipate that NHSK papers can find applications in sensors, electrochemical devices and coatings.

MATERIALS AND METHODS

Materials. SWCNT were high-purity grade high-pressure carbon monoxide (HiPCO) tubes purchased from Unidym, batch no. P0288. Tube diameters were found to be in the range of 1.0−1.6 nm from the G-band and radial breathing modes using Raman spectroscopy. The PE used in this study was a high-density PE (HDPE) purchased from Aldrich (melt flow index, 12 g/10 min). Spectrophotomeric grade *ortho*-dichlorobenzene (DCB) was purchased from Aldrich and used as received. Deionized water was purchased from Aqua Solutions. Silver paint was used as received from SPI supplies.

Formation of NHSK and NHSK Paper Preparation. PE NHSKs were fabricated following the literature procedure[21] incorporating some modifications for process optimization, specifically, the addition of alcohol to the SWCNT suspension and centrifugation of the SWCNT to remove bundles prior to crystallization. In brief, SWCNT were ultrasonicated in a solution of DCB at 40 °C for 2 h to produce an exfoliated dispersion. Niyogi *et al.* showed[64] that sonication of solutions of CNT in DCB can achieve stable exfoliation of the nanotubes through an irreversible polymerization of DCB by the formation of free radicals. We have found this DCB sonopolymer to interfere with NHSK growth. To avoid this side-reaction, DCB sonopolymer free radicals were quenched by the addition of 3 wt % ethanol (99% purity, used as received from Aldrich) into the reaction mixture. After sonication, the solution was centrifuged at 10 000 rpm for 20 min and the supernatant was collected. Separately, PE pellets were dissolved in DCB at 130 °C. The temperatures of the two solutions were equilibrated at 130 °C before mixing. The mixture was then cooled to 88.5 °C to induce heterogeneous crystallization of PE. The final concentration of SWCNT in solution was approximately 0.01% by weight; the PE concentration was varied from 0.002 to 0.2 wt %. Crystallization was allowed to proceed for 60 min. Isothermal filtration of the solution was then performed to remove any remaining uncrystallized polymer, leaving NHSK in solution.

To produce thick films, the NHSK solutions were filtered through 0.2 μm polytetrafluoroethylene (PTFE) membranes from Savillex. The films were rinsed with methanol three times after filtering. After drying in a vacuum desiccator for at least two days, PTFE membrane-mounted NHSK paper was obtained, which could then be peeled off this membrane to produce stable free-standing films as desired. Raman spectroscopy of NHSK materials showed that the D/G peak intensity ratio was unchanged after the NHSK functionalization and vacuum deposition process, indicating that the SWCNTs were not significantly damaged throughout the procedure. Films were mounted on glass slides with double-sided tape for CA measurements. The annealing of films was done on a hot stage at 180 °C for 60 s. A glass coverslip was used to keep the films flat during the annealing process; no effort was otherwise made to press the films. Annealed films were immediately quenched in liquid nitrogen.

Characterization. Conductivities of samples were tested using a PARSTAT 2273 potentiostat/galvanostat in four-point probe configuration. Electrical contacts were painted on using conductive silver paint from SPI supplies.

CA measurements using the sessile drop method were carried out on a three-axis horizontal tilt stage on an optical table. Determination of CA was performed using the ImageJ software package. Deionized water was used for the CA of NHSK paper before and after annealing on a precision hot stage. The static CA was determined as an average of at least eight measurements of 2 μL droplets, with uncertainty calculated using the standard deviation. Nonstationary CA measurements were performed using a range of conditions as needed. Advancing CAs were measured using video recordings of the droplets as the volume was increased. Receding CA values were found by monitoring the evaporation of water droplets. Droplet sliding angles were found using a similar setup, with video recordings of 50 μL droplets.

To determine the PE contents of samples, thermogravimetric analysis (TGA) was performed on each of the buckypaper. Scans were run on a PerkinElmer TGA 7 under air, from 50−950 °C at a scan rate of 20 °C min^{-1}. Sample mass concentrations were calculated based on the derivative of the TGA curve: the contributions from the individual components (PE or SWCNT) to the overall mass were obtained by deconvoluting the peaks of this mixture in the temperature range of degradation of this material, and then integrating each peak. The error was taken as the instrument uncertainty. Differential scanning calorimetry (DSC) was done on a PerkinElmer DSC 7 under nitrogen. The scan rate was 10 °C/min, and the sample was taken from 20 to 180 °C, then cooled to −65 °C, and then heated back to 180 °C.

SEM micrographs were taken using a Zeiss Supra 50VP SEM in high-vacuum mode. NHSK samples were prepared by spin-coating on a glass coverslip. SWCNT and NHSK films were prepared by mounting films on an SEM stub using conductive carbon tape from SPI supplies. Edge-on surfaces of these films were prepared by freeze fracture at liquid nitrogen temperatures. Prior to imaging, samples were conformally coated from an 80/20% Pt/Pd target using a Cressington sputter coater at 40 mA under argon. All micrographs were taken using a 30 μm aperture and a 1 keV beam.

Small angle X-ray scattering (SAXS) was performed on a Rigaku S-MAX3000 pinhole SAXS camera with a three meter detector and a Cu Kα source. Film samples were sectioned into half-millimeter strips and stacked to form a target such that the thickness was adequate for in-plane measurements. Through-plane

patterns were produced by placing the strips flat against the pinhole. In-plane diffraction patterns were taken by mounting the samples so that they were slightly misaligned and incrementally rotating them about the *x*-axis. The orientation corresponding to maximum diffraction anisotropy was taken as the in-plane diffraction.

Profilometry was performed on a Zygo NewView 6000 optical profiler with 0.1 nm height resolution and 15000 μm range. Samples were scanned over 0.5×0.7 mm regions, and 10 linescans of 0.1 mm were analyzed to estimate the surface roughness properties. Gas adsorption analysis was performed using Quantachrome Instruments (U.S.A.) Quadrasorb with N_2 adsorbate at $-196\ °C$ after 48 h degassing at room temperature. BET surface area was calculated using the adsorption branch.

Conflict of Interest: The authors declare no competing financial interest.

Supporting Information Available: A more detailed description of the formation method for NHSK batches, data analysis, and histograms of the diameters and intra-NHSK spacings of the various NHSK batches used in the study, profilometry and microscale roughness calculation, thermogravimetric analysis curves, and differential scanning calorimetry thermograms of bulk PE and NHSK films. This material is available free of charge *via* the Internet at http://pubs.acs.org.

REFERENCES AND NOTES

1. Zhao, B.; Futaba, D. N.; Yasuda, S.; Akoshima, M.; Yamada, T.; Hata, K. Exploring Advantages of Diverse Carbon Nanotube Forests with Tailored Structures Synthesized by Supergrowth from Engineered Catalysts. *ACS Nano* **2009**, *3*, 108–114.
2. Meitl, M. A.; Zhou, Y. X.; Gaur, A.; Jeon, S.; Usrey, M. L.; Strano, M. S.; Rogers, J. A. Solution Casting and Transfer Printing Single-Walled Carbon Nanotube Films. *Nano Lett.* **2004**, *4*, 1643–1647.
3. Wu, Z. C.; Chen, Z. H.; Du, X.; Logan, J. M.; Sippel, J.; Nikolou, M.; Kamaras, K.; Reynolds, J. R.; Tanner, D. B.; Hebard, A. F.; *et al.* Transparent, Conductive Carbon Nanotube Films. *Science* **2004**, *305*, 1273–1276.
4. Cambaz, Z. G.; Yushin, G.; Osswald, S.; Mochalin, V.; Gogotsi, Y. Noncatalytic Synthesis of Carbon Nanotubes, Graphene and Graphite on SiC. *Carbon* **2008**, *46*, 841–849.
5. Abe, Y.; Tomuro, R.; Sano, M. Highly Efficient Direct Current Electrodeposition of Single-Walled Carbon Nanotubes in Anhydrous Solvents. *Adv. Mater.* **2005**, *17*, 2192–2194.
6. Zhang, X. W. Hydroentangling: A Novel Approach to High-Speed Fabrication of Carbon Nanotube Membranes. *Adv. Mater.* **2008**, *20*, 4140–4144.
7. Giancane, G.; Ruland, A.; Sgobba, V.; Manno, D.; Serra, A.; Farinola, G. M.; Omar, O. H.; Guldi, D. M.; Valli, L. Aligning Single-Walled Carbon Nanotubes by Means of Langmuir–Blodgett Film Deposition: Optical, Morphological, and Photo-electrochemical Studies. *Adv. Funct. Mater.* **2010**, *20*, 2481–2488.
8. Li, X.; Zhang, L.; Wang, X.; Shimoyama, I.; Sun, X.; Seo, W.-S.; Dai, H. Langmuir–Blodgett Assembly of Densely Aligned Single-Walled Carbon Nanotubes from Bulk Materials. *J. Am. Chem. Soc.* **2007**, *129*, 4890–4891.
9. Small, W. R.; Masdarolomoor, F.; Wallace, G. G.; Panhuis, M. Inkjet Deposition and Characterization of Transparent Conducting Electroactive Polyaniline Composite Films with a High Carbon Nanotube Loading Fraction. *J. Mater. Chem.* **2007**, *17*, 4359–4361.
10. Song, J. W.; Han, C. S. Inkjet Printing of Single Walled Carbon Nanotubes. *Int. J. Precis. Eng. Manuf.* **2008**, *9*, 79–81.
11. Lau, K. K. S.; Bico, J.; Teo, K. B. K.; Chhowalla, M.; Amaratunga, G. A. J.; Milne, W. I.; McKinley, G. H.; Gleason, K. K. Superhydrophobic Carbon Nanotube Forests. *Nano Lett.* **2003**, *3*, 1701–1705.
12. de Heer, W. A.; Bacsa, W. S.; Chatelain, A.; Gerfin, T.; Humphreybaker, R.; Forro, L.; Ugarte, D. Aligned Carbon Nanotube Films - Production and Optical and Electronic Properties. *Science* **1995**, *268*, 845–847.
13. Zbib, A. A.; Mesarovic, S. D.; Lilleodden, E. T.; McClain, D.; Jiao, J.; Bahr, D. F. The Coordinated Buckling of Carbon Nanotube Turfs Under Uniform Compression. *Nanotechnology* **2008**, *19*, 7.
14. Hutchens, S. B.; Hall, L. J.; Greer, J. R. In situ Mechanical Testing Reveals Periodic Buckle Nucleation and Propagation in Carbon Nanotube Bundles. *Adv. Funct. Mater.* **2010**, *20*, 2338–2346.
15. Futaba, D. N.; Hata, K.; Yamada, T.; Hiraoka, T.; Hayamizu, Y.; Kakudate, Y.; Tanaike, O.; Hatori, H.; Yumura, M.; Iijima, S. Shape-Engineerable and Highly Densely Packed Single-Walled Carbon Nanotubes and Their Application as Supercapacitor Electrodes. *Nat. Mater.* **2006**, *5*, 987–994.
16. Li, C. Y. Polymer Single Crystal Meets Nanoparticles. *J. Polym. Sci. Polym. Phys.* **2009**, *47*, 2436–2440.
17. Li, B.; Li, C. Y. Immobilizing Au Nanoparticles with Polymer Single Crystals, Patterning and Asymmetric Functionalization. *J. Am. Chem. Soc.* **2007**, *129*, 12–13.
18. Wang, B. B.; Li, B.; Xiong, J.; Li, C. Y. Hierarchically Ordered Polymer Nanofibers *via* Electrospinning and Controlled Polymer Crystallization. *Macromolecules* **2008**, *41*, 9516–9521.
19. Wang, B. B.; Li, B.; Zhao, B.; Li, C. Y. Amphiphilic Janus Gold Nanoparticles *via* Combining "Solid-State Grafting-to" and "Grafting-from" Methods. *J. Am. Chem. Soc.* **2008**, *130*, 11594–11595.
20. Chen, X.; Dong, B.; Wang, B. B.; Shah, R.; Li, C. Y. Crystalline Block Copolymer Decorated, Hierarchically Ordered Polymer Nanofibers. *Macromolecules* **2010**, *43*, 9918–9927.
21. Li, C. Y.; Li, L. Y.; Cai, W. W.; Kodjie, S. L.; Tenneti, K. K. Nanohybrid Shish-Kebabs: Periodically Functionalized Carbon Nanotubes. *Adv. Mater.* **2005**, *17*, 1198–1202.
22. Li, L.; Li, B.; Hood, M. A.; Li, C. Y. Carbon Nanotube Induced Polymer Crystallization: The Formation of Nanohybrid Shish Kebabs. *Polymer* **2009**, *50*, 953–965.
23. Zwijnenburg, A.; Pennings, A. J. Longitudinal Growth of Polymer Crystals from Flowing Solutions. IV. The Mechanical Properties of Fibrillar Polyethylene Crystals. *J. Polym. Sci.: Polym. Lett. Ed.* **1976**, *14*, 339–346.
24. Smook, J.; Pennings, A. J. Elastic Flow Instabilities and Shish-Kebab Formation During Gel-Spinning of Ultrahigh Molecular Weight Polyethylene. *J. Mater. Sci.* **1984**, *19*, 31–43.
25. Somani, R. H.; Yang, L.; Zhu, L.; Hsiao, B. S. Flow-Induced Shish-Kebab Precursor Structures in Entangled Polymer Melts. *Polymer* **2005**, *46*, 8587–8623.
26. Li, L. Y.; Li, C. Y.; Ni, C. Y. Polymer Crystallization-Driven, Periodic Patterning on Carbon Nanotubes. *J. Am. Chem. Soc.* **2006**, *128*, 1692–1699.
27. Li, L.; Yang, Y.; Yang, G.; Chen, X.; Hsiao, B. S.; Chu, B.; Spanier, J. E.; Li, C. Y. Patterning Polyethylene Oligomers on Carbon Nanotubes Using Physical Vapor Deposition. *Nano Lett.* **2006**, *6*, 1007–1012.
28. Li, L.; Wang, W.; Laird, E. D.; Li, C. Y.; Defaux, M.; Ivanov, D. A. Polyethylene/Carbon Nanotube Nano Hybrid Shish-Kebab Obtained by Solvent Evaporation and Thin-Film Crystallization. *Polymer* **2011**, *52*, 3633–3638.
29. Li, B.; Li, L.; Wang, B.; Li, C. Y. Alternating Patterns on Single-walled Carbon Nanotubes. *Nature Nanotechnol.* **2009**, *4*, 358–362.
30. Li, L. Y.; Li, B.; Yang, G. L.; Li, C. Y. Polymer Decoration on Carbon Nanotubes *via* Physical Vapor Deposition. *Langmuir* **2007**, *23*, 8522–8525.
31. Zhang, F.; Zhang, H.; Zhang, Z. W.; Chen, Z. M.; Xu, Q. Modification of Carbon Nanotubes: Water-Soluble Polymers Nanocrystal Wrapping to Periodic Patterning with Assistance of Supercritical CO_2. *Macromolecules* **2008**, *41*, 4519–4523.

32. Miltner, H. E.; Grossiord, N.; Lu, K. B.; Loos, J.; Koning, C. E.; Van Mele, B. Isotactic Polypropylene/Carbon Nanotube Composites Prepared by Latex Technology. Thermal Analysis of Carbon Nanotube-Induced Nucleation. *Macromolecules* **2008**, *41*, 5753–5762.

33. Zhang, S.; Minus, M. L.; Zhu, L. B.; Wong, C. P.; Kumar, S. Polymer Transcrystallinity Induced by Carbon Nanotubes. *Polymer* **2008**, *49*, 1356–1364.

34. Limpert, E.; Stahel, W. A.; Abbt, M. Log-Normal Distributions Across the Sciences: Keys and Clues. *Bioscience* **2001**, *51*, 341–352.

35. Pujari, S.; Rahatekar, S. S.; Gilman, J. W.; Koziol, K. K.; Windle, A. H.; Burghardt, W. R. Orientation Dynamics in Multiwalled Carbon Nanotube Dispersions Under Shear Flow. *J. Chem. Phys.* **2009**, *130*, 1–9.

36. Kakudo, M.; Kasai, N. *X-ray Diffraction by Polymers*; Elsevier: Tokyo, 1972; p 231−257.

37. Mattia, D.; Ban, H. H.; Gogotsi, Y. Wetting of CVD Carbon Films by Polar and Nonpolar Liquids and Implications for Carbon Nanopipes. *Langmuir* **2006**, *22*, 1789–1794.

38. Mattia, D.; Rossi, M. P.; Kim, B. M.; Korneva, G.; Bau, H. H.; Gogotsi, Y. Effect of Graphitization on the Wettability and Electrical Conductivity of CVD-Carbon Nanotubes and Films. *J. Phys. Chem. B* **2006**, *110*, 9850–9855.

39. Ma, M. L.; Gupta, M.; Li, Z.; Zhai, L.; Gleason, K. K.; Cohen, R. E.; Rubner, M. F.; Rutledge, G. C. Decorated Electrospun Fibers Exhibiting Superhydrophobicity. *Adv. Mater.* **2007**, *19*, 255–259.

40. Feng, X.; Jiang, L. Design and Creation of Superwetting/Antiwetting Surfaces. *Adv. Mater.* **2006**, *18*, 3063–3078.

41. Liu, H.; Zhai, J.; Jiang, L. Wetting and Anti-wetting on Aligned Carbon Nanotube Films. *Soft Matter* **2006**, *2*, 811–821.

42. Caps, H.; Vandormael, D.; Loicq, J.; Dorbolo, S.; Vandewalle, N. Hybrid Wetting State on Micro-waffle Textures. *Europhys. Lett.* **2009**, *88*), 16002 1–4.

43. Xia, F.; Jiang, L. Bio-Inspired, Smart, Multiscale Interfacial Materials. *Adv. Mater.* **2008**, *20*, 2842–2858.

44. Feng, L.; Zhang, Y. A.; Xi, J. M.; Zhu, Y.; Wang, N.; Xia, F.; Jiang, L. Petal Effect: A Superhydrophobic State with High Adhesive Force. *Langmuir* **2008**, *24*, 4114–4119.

45. Jeong, H. E.; Lee, S. H.; Kim, J. K.; Suh, K. Y. Nanoengineered Multiscale Hierarchical Structures with Tailored Wetting Properties. *Langmuir* **2006**, *22*, 1640–1645.

46. Jeong, H. E.; Kwak, M. K.; Park, C. I.; Suh, K. Y. Wettability of Nanoengineered Dual-Roughness Surfaces Fabricated by UV-Assisted Capillary Force Lithography. *J. Colloid Interface Sci.* **2009**, *339*, 202–207.

47. Park, C. I.; Jeong, H. E.; Lee, S. H.; Cho, H. S.; Suh, K. Y. Wetting Transition and Optimal Design for Microstructured Surfaces with Hydrophobic and Hydrophilic Materials. *J. Colloid Interface Sci.* **2009**, *336*, 298–303.

48. Schonhorn, H. a. R.; Frank, W. Wettability of Polyethylene Single Crystal Aggregates. *J. Phys. Chem.* **1966**, *70*, 3811–3815.

49. Erbil, H. Y.; McHale, G.; Rowan, S. M.; Newton, M. I. Determination of the Receding Contact Angle of Sessile Drops on Polymer Surfaces by Evaporation. *Langmuir* **1999**, *15*, 7378–7385.

50. Gao, L. C.; McCarthy, T. J. Contact Angle Hysteresis Explained. *Langmuir* **2006**, *22*, 6234–6237.

51. Norton, Robert L. *Machine Design: An Integrated Approach*, 3rd ed; Prentice Hall: Upper Saddle River, NJ, 2005.

52. Izadi-Najafabadi, A.; Yasuda, S.; Kobashi, K.; Yamada, T.; Futaba, D. N.; Hatori, H.; Yumura, M.; Iijima, S.; Hata, K. Extracting the Full Potential of Single-Walled Carbon Nanotubes as Durable Supercapacitor Electrodes Operable at 4 V with High Power and Energy Density. *Adv. Mater.* **2010**, *22*, E235–E241.

53. Updike, S. J.; Hicks, G. P. The Enzyme Electrode. *Nature* **1967**, *214*, 986–988.

54. Heng, L. Y.; Chou, A.; Yu, J.; Chen, Y.; Gooding, J. J. Demonstration of the Advantages of Using Bamboo-like Nanotubes for Electrochemical Biosensor Applications Compared with Single Walled Carbon Nanotubes. *Electrochem. Commun.* **2005**, *7*, 1457–1462.

55. Green, M. J.; Behabtu, N.; Pasquali, M.; Adams, W. W. Nanotubes as Polymers. *Polymer* **2009**, *50*, 4979–4997.

56. Bryning, M. B.; Islam, M. F.; Kikkawa, J. M.; Yodh, A. G. Very Low Conductivity Threshold in Bulk Isotropic Single-Walled Carbon Nanotube−Epoxy Composites. *Adv. Mater.* **2005**, *17*, 1186–1191.

57. Stauffer, D.; Aharony, A. *Introduction to Percolation*; Taylor and Francis: London, 1992.

58. Trionfi, A.; Wang, D. H.; Jacobs, J. D.; Tan, L. S.; Vaia, R. A.; Hsu, J. W. P. Direct Measurement of the Percolation Probability in Carbon Nanofiber−Polyimide Nanocomposites. *Phys. Rev. Lett.* **2009**, *102*, 116601.

59. Balberg, I.; Azulay, D.; Millo, O.; Ambrosetti, G.; Grimaldi, C. Comment on "Direct Measurement of the Percolation Probability in Carbon Nanofiber−Polyimide Nanocomposites". *Phys. Rev. Lett.* **2011**, *106*, 079701.

60. Hsu, J. W. P.; Vaia, R. A.; Trionfi, A. Comment on "Direct Measurement of the Percolation Probability in Carbon Nanofiber-Polyimide Nanocomposites" Reply. *Phys. Rev. Lett.* **2011**, *106*, 079702.

61. Haggenmueller, R.; Guthy, C.; Lukes, J. R.; Fischer, J. E.; Winey, K. I. Single Wall Carbon Nanotube/Polyethylene Nanocomposites: Thermal and Electrical Conductivity. *Macromolecules* **2007**, *40*, 2417–2421.

62. Jeon, K.; Lumata, L.; Tokumoto, T.; Steven, E.; Brooks, J.; Alamo, R. G. Low Electrical Conductivity Threshold and Crystalline Morphology of Single-Walled Carbon Nanotubes—High Density Polyethylene Nanocomposites Characterized by SEM, Raman Spectroscopy, and AFM. *Polymer* **2007**, *48*, 4751–4764.

63. Du, F. M.; Fischer, J. E.; Winey, K. I. Effect of Nanotube Alignment on Percolation Conductivity in Carbon Nanotube/Polymer Composites. *Phys. Rev. B* **2005**, *72*, 12140.

64. Niyogi, S.; Hamon, M. A.; Perea, D. E.; Kang, C. B.; Zhao, B.; Pal, S. K.; Wyant, A. E.; Itkis, M. E.; Haddon, R. C. Ultrasonic Dispersions of Single-Walled Carbon Nanotubes. *J. Phys. Chem. B* **2003**, *107*, 8799–8804.